catalysts

MDPI

Review

Electrochemical CO_2 Reduction to CO Catalyzed by 2D Nanostructures

Chaitanya B. Hiragond [1], Hwapyong Kim [1], Junho Lee [1], Saurav Sorcar [1], Can Erkey [2] and Su-Il In [1,3,*]

1 Department of Energy Science & Engineering, DGIST, 333 Techno Jungang-daero, Hyeonpung-eup, Dalseong-gun, Daegu 42988, Korea; chetan123@dgist.ac.kr (C.B.H.); khp911@dgist.ac.kr (H.K.); dlwnsgh95@dgist.ac.kr (J.L.); sorcar@dgist.ac.kr (S.S.)

2 Chemical and Biological Engineering Department, Koç University, 34450 Sarıyer, Turkey; CERKEY@ku.edu.tr

3 Linde + Robinson Laboratories, California Institute of Technology, Pasadena, CA 91125, USA

* Correspondence: insuil@dgist.ac.kr; Tel.: +82-53-785-6417

Received: 7 December 2019; Accepted: 5 January 2020; Published: 9 January 2020

Abstract: Electrochemical CO_2 reduction towards value-added chemical feedstocks has been extensively studied in recent years to resolve the energy and environmental problems. The practical application of electrochemical CO_2 reduction technology requires a cost-effective, highly efficient, and robust catalyst. To date, vigorous research have been carried out to increase the proficiency of electrocatalysts. In recent years, two-dimensional (2D) graphene and transition metal chalcogenides (TMCs) have displayed excellent activity towards CO_2 reduction. This review focuses on the recent progress of 2D graphene and TMCs for selective electrochemical CO_2 reduction into CO.

Keywords: electrochemical CO_2 reduction; 2D nanostructures; MoS_2; graphene; WSe_2

1. Introduction

The increasing utilization of fossil fuels leads to huge amounts of CO_2 emissions which causes inevitable damage to the planet's ecosystem [1–5]. One possible way to counter this is to capture and convert CO_2 to industrially important organic compounds [6–10]. To date, several strategies have been employed for the reduction of CO_2; for example, chemical [11], thermochemical [12,13], photocatalytic [14–21], electrocatalytic [22–24], biological [25], and inorganic transformation [26]. However, among those, a great deal of research has focused on electrochemical CO_2 reduction technology aimed towards large scale applications due to its environmental compatibility and cost-effectiveness [27–29].

However, the low reactivity of CO_2 requires high energy input for its activation [30–34]. CO_2 can be reduced to various useful products by employing suitable cell potential in combination with appropriate catalysts (as shown in Table 1 (Equations (1)–(7)) [35,36]. For example, CO_2 reduction to C_1 products such as CO is thermodynamically more favorable because it requires only two electrons and two protons for the activation, and such C_1 products are useful as building blocks for the production of higher hydrocarbons [37]. In contrast, long-chain hydrocarbons are industrially significant but CO_2 reduction to higher hydrocarbons is a complex process, since C–C bond formation demands high energy input [38]. Hence, rather than CO_2 reduction to higher hydrocarbons, the product selectivity and efficiency are crucial factors to be addressed.

Table 1. The standard redox potentials for the main products of CO_2 reduction in aqueous solution.

Half−Electrochemical Thermodynamic Reactions	Product	E° Redox	Equation
$CO_2 + e^- \rightarrow CO_2^{\bullet}$	CO_2 anion radical	−1.90 V	(1)
$CO_2 + 2H^+ + 2e^- \rightarrow HCOOH$	Formic acid	−0.61 V	(2)
$CO_2 + 2H^+ + 2e^- \rightarrow CO + H_2O$	Carbon monoxide	−0.53 V	(3)
$CO_2 + 4H^+ + 4e^- \rightarrow HCHO + H_2O$	Formaldehyde	−0.48 V	(4)
$CO_2 + 6H^+ + 6e^- \rightarrow CH_3OH + H_2O$	Methanol	−0.38 V	(5)
$CO_2 + 8H^+ + 8e^- \rightarrow CH_4 + 2H_2O$	Methane	−0.24 V	(6)
$2CO_2 + 12H^+ + 12e^- \rightarrow C_2H_4 + 4H_2O$	Ethylene	−0.41 V	(7)

However, developing a low cost, highly efficient, and stable catalyst remains an obstacle to be overcome. To date a number of catalysts including metals [39], alloys [40], metal oxides [41,42], metal complexes [43], carbides [44,45], and metal-organic frameworks [46–48] have been studied for electrocatalytic CO_2 reduction. Of these, transition metal-based catalysts (e.g., Au, Pt, Ni, and Ag) displayed notable activity, but their scarcity in nature and high-cost limit them from large-scale employment [49]. Metal oxides, namely, TiO_2, RuO_2, and IrO_2, have been widely investigated [50–52], but they also possess notable disadvantages—low efficiency, high cost, poor stability, and low current exchange density. Recently 2D materials, in particular, graphene derivatives and transition metal chalcogenides (TMCs), have emerged as active and inexpensive alternatives to traditional electrocatalysts [52]. They possess unique physicochemical properties and their large surface areas facilitate the redox reaction process to boost the catalytic activity [53,54]. Moreover, exposed active sites of 2D nanostructures are favorable for interfacial charge transfer [55]. Enhancement in mass transport and electron conductivity of 2D electrocatalysts can be achieved by co-catalyst doping [56]. For instance, doping of Nb into MoS_2 increases the overall catalytic performance at the minimal potential of 50–150 mV [57]. Therefore, all these collective advantages of 2D nanostructures make them suitable for electrochemical CO_2 reduction.

This short review will describe the recent progress and advances in emerging 2D materials in electrochemical CO_2 reduction towards CO production. We will be discussing the fundamentals and pathways of electrochemical CO_2 reduction. Various advanced synthesis methodologies of 2D catalysts and the effect of metal/and non-metal doping on catalytic activity will also be discussed along with the theoretical studies.

2. Fundamentals of Electrochemical CO_2 Reduction

CO_2 is a linear molecule and a large input of energy is needed to break the carbon and oxygen bonding (i.e., C=O) [58,59]. H_2O reduction to H_2 and $\frac{1}{2}O_2$ demands 237.2 kJ mol^{-1} of energy under standard conditions. Whereas, CO_2 reduction to hydrocarbon fuels CH_4 and CH_3OH requires much higher free energy towards positive change, equivalent to 818.3 kJ mol^{-1} and 702 kJ mol^{-1}, respectively [59]. Therefore, CO_2 reduction is an uphill reaction and considered as a grand challenge [60]. The electrochemical cell used for CO_2 reduction reaction consists of a cathode, an anode, and an ion-exchange membrane placed in-between them, as demonstrated in Figure 1. The process of electrochemical CO_2 reduction begins with diffusion of CO_2 molecule from the solution to cathode surface which is coated with a suitable catalyst. One of the postulated mechanisms for activating CO_2 molecule is a single electron transfer to CO_2, thereby generating a $CO_2^{\bullet-}$ radical anion [61]. A single-electron addition bends the linear molecule because of the repulsion between acquired electron over electrophilic carbon atom and free electron pairs on the oxygen atom. However, this mechanism has a setback, because for such a process to take place, a very high redox potential is required (i.e., −1.9 V versus NHE) [62]. But then, as seen in Table 1, which depicts the standard redox potential for CO_2 reduction reactions, the possibility of single-electron transfer to a CO_2 molecule becomes inconceivable [63]. In terms of thermodynamics, the edges of conduction band and valence band of a

semiconductor must be above and below the standard reduction and oxidation potentials, respectively. Therefore, this makes it quite clear why a single electron transfer to the CO_2 molecule is highly improbable. Hence, a better efficiency can be achieved with a multiple proton-coupled electron transfer (PCET) process. This process involves the transfer of protons with electrons, thereby bypassing the formation of high energy $CO_2^{\bullet}$ radical [64]. Even though the PCET phenomenon makes CO_2 reduction feasible, the process is dependent upon the concentration of available electrons and protons. For example, as manifested from Equations (2)–(7), which show the main products obtained during CO_2 reduction in the presence of H_2O, by the PCET phenomenon (pH = 7) [65], generation of formic acid and carbon monoxide is more favorable than generating methane. The reason behind such a phenomenon is that the carbon monoxide requires two electrons and protons, whereas eight electrons and protons are necessary for producing methane. Another possible pathway involved in CO_2 reduction to CO is decoupled electron-proton transfer, where the CO production can be carried out by the formation of a CO_2^{2-} radical [55]. However, theoretical studies and quantum chemical calculations provide a better understanding of the mechanism and reaction pathway of electrochemical CO_2 reduction. For example, the computational hydrogen electrode (CHE) model is one of the most convenient and widely employed methods for the PCET process [66]. Paterson et al. reported a CHE model for electrochemical CO_2 reduction on the metallic copper electrode and it has been found that metal electrodes can easily generate hydrocarbon products upon CO_2 reduction [67,68]. On the other hand, the natures of the catalysts used for catalytic reaction play important roles in the reaction pathway.

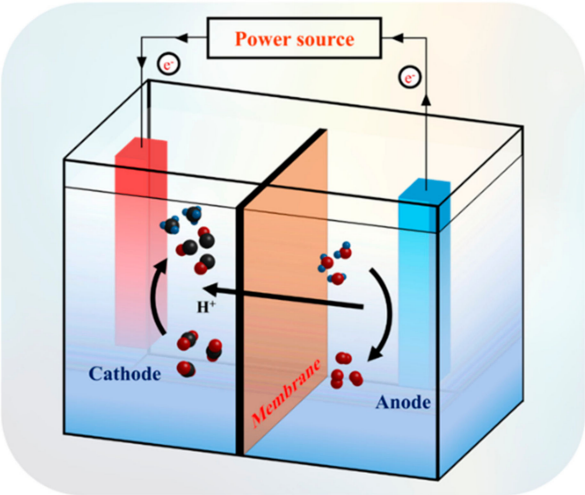

Figure 1. Schematic diagram showing the illustration of CO_2 reduction to chemical fuels using an electrochemical cell.

Another challenge in electrochemical CO_2 reduction is competition with proton reduction, i.e., hydrogen evolution reaction (HER), because it is a two-electron and proton process, requiring far less energy [69]. This leads to poor selectivity to carbonaceous products. Last but not the least, CO_2 has very low solubility in an aqueous medium (≈0.034 M), which negatively affects the overall CO_2 reduction activity to chemical fuels. There are efforts to overcome this solubility problem by using gas diffusion layers to use the polymer electrolytes. In conclusion, both thermodynamic and kinetic barriers for the transformation to value-added fuels make it a challenging reaction. In the anode half of the electrochemical cell, oxygen evolution takes place. Lastly, the ion exchange membrane functions through avoiding oxidation of carbonaceous products by acting as a barrier to prevent the flow of electrons and allowing passage of protons only. A schematic of the electrochemical cell and reactions going on is shown in Figure 1, with the following key points:

a. CO_2 adsorption on cathode surface;
b. PCET process;

c. Desorption of products formed from the cathode surface.

2.1. Parameters of Electrochemical CO_2 Reduction

To examine the utility of electrochemical CO_2 reaction there have been key parameters set that include current density (j), overpotential (η), faradaic efficiency (FE), turnover frequency (TOF), effect of electrolyte, and stability. Those parameters will be discussed in this section, which will assist the readers with understanding the concepts and applying them while evaluating their experiments pertaining to electrochemical CO_2 reduction in the laboratory.

2.1.1. Current Density (j)

Current density is an important parameter for evaluating the activity of electrochemical CO_2 reduction. Application of a constant cell voltage gives rise to electrolysis current. Therefore, current density (j) is described as the ratio between current (i) and the geometric surface area of working electrode (A), as shown in Equation (8).

$$j = \frac{i}{A} \tag{8}$$

2.1.2. Faradaic Efficiency (FE)

Faradaic efficiency is yet another important guideline with which to evaluate the amount of product cross-over and electrochemical selectivity of CO_2 reduction reaction [70]. It is given as the ratio of the charge from total product generated (αNF, whereas α is the number of electrons transferred, N is the amount of desired product's moles, and F is the faraday constant 96,485 C mol^{-1}) to the total amount of charges passed during the electrolysis (Q), as shown in Equation (9) [55]. It also correlates with the selectivity of products during CO_2 reduction.

$$E_{faradaic} = \frac{\alpha NF}{Q} \tag{9}$$

2.1.3. Overpotential (η)

The difference between the actual required potential and the equilibrium potential is expressed as overpotential. An electrocatalyst showcasing low overpotential is considered to show a better and efficient catalytic activity. Overpotential is calculated by the difference between the standard potential of the reaction of CO_2 and the reduced product (E_{eq}), and actual electrode potential (E), as shown in Equation (10) [71].

$$\eta = E - E_{eq} \tag{10}$$

2.1.4. Turnover Frequency (TOF)

It is determined as the number of CO_2 conversion products obtained over number of active sites per unit time. The catalyst with a high turnover frequency means it possess many innate active sites, which in turn, provide better activity. TOF is calculated by the ratio of the number of moles of the target product produced per unit time (N_p) to the maximum number of moles of the active site of the catalyst (N_c), as shown in Equation (11) [71].

$$TOF = \frac{N_p}{N_c} \tag{11}$$

2.1.5. Effect of Electrolyte

The product selectivity can be altered/controlled by varying the electrolyte solution in electrochemical CO_2 reduction reaction [72]. To date, various types of electrolytes have been used, such as non-aqueous (organic) solvents, aqueous and ionic liquids. Among them, aqueous electrolytes

are cheap, environmentally friendly, and possess high sustainability. Moreover, in aqueous electrolytes, the concentration, pH value, and buffer capacity are of equal importance for eventually affecting the efficiency and product selectivity [73]. CO_2 is highly soluble in organic electrolytes, but they are toxic, expensive and require large overpotentials compared to aqueous electrolytes. The ionic liquids are polar in nature which further helps to improve the conductivity and solubility of CO_2.

2.1.6. Stability

Stability is one of the most important criteria in order to commercialize a catalyst. Therefore, even if a catalyst has high efficiency, it is equally as important to have long term stability.

3. 2D Electrocatalysts

The 2D materials possess excellent structural and morphological features, as shown in Figure 2. In the following sections, we will briefly describe the various 2D electrocatalysts for CO_2 reduction into CO.

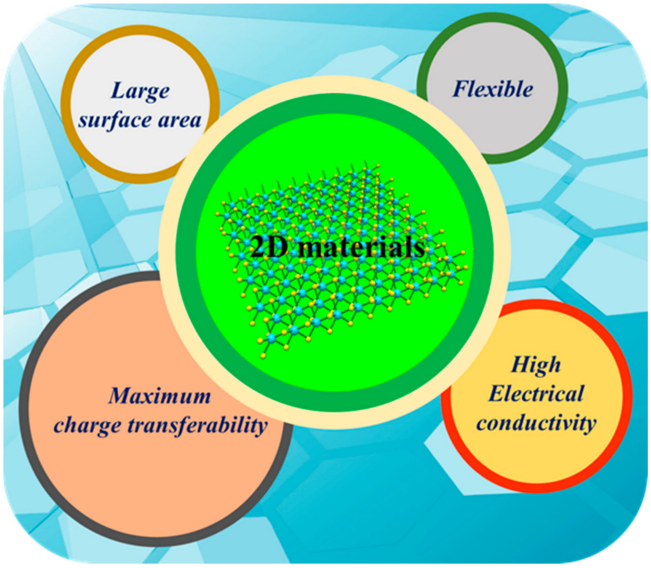

Figure 2. Schematics showing the properties of 2D materials.

3.1. 2D Molybdenum (Mo) Transition Metal Dichalcogenides (TMDCs)

It is commonly known that the defects, edge sites, and dopants present with a catalyst greatly influence the activity of electrochemical CO_2 reduction. In recent years, 2D MoS_2 has shown great potential because of its unique physicochemical and structural properties. Asadi et al. reported bulk MoS_2 with a layer-stacked structure for electrocatalytic CO_2 reduction to produce CO [74]. STEM (Scanning transmission electron microscopy) investigation confirmed the presence of vertically aligned multi-layered sheets of MoS_2 flakes. Remarkably, as-obtained metal terminated edges of MoS_2 were considered reactive sites for electrocatalytic CO_2 reduction. Excellent faradic efficiency of 98% was achieved with a high current density operated at a minimal overpotential of 54 mV. Therein, the presence of H^+ from the water molecule (in electrolyte solution) and electron generated on the catalyst's surface contribute to the reduction of CO_2 to form CO. Density functional theory (DFT) studies revealed that the presence of MoS_2 edge sites and metallic character of Mo atoms were collectively responsible for high catalytic activity and stability over 10 h. That theoretical study, significantly, provides a new idea for the experimental fabrication of a competent electrocatalyst. In another example, Nørskov et al. improved catalytic performance by breaking the linear scaling relationship among *CO, *CHO, and *COOH intermediates at the edge sites of MoS_2 and $MoSe_2$ [56]. Furthermore, in another study NÒrskov and coworkers demonstrated that transition metal-doped MoS_2 significantly improved the catalytic

activity [75]. Product selectivity mainly depends upon binding energies of edge sites present over the catalyst. For example, S edges of Ni-doped MoS_2 and Mo edges of $MoSe_2$ selectively produce CO. However, S edges of undoped MoS_2 are selective towards H_2 formation.

In 2016, Abbasi and coworkers reported Nb-doped vertically aligned MoS_2 electrocatalyst for CO_2 reduction into CO [57]. A small shift in Raman and XPS spectra confirmed Nb doping in MoS_2 (Figure 3A,B). The CO_2 reduction experiment was performed in an electrochemical cell by employing cyclic voltammetry at a -0.8 ± 1.0 V potential range. All tests were performed in an electrolyte solution composed of a CO_2 saturated, 50:50 vol% mixture of 1-ethyl-3-methylimidazolium tetrafluoroborate (EMIM-BF_4) and deionized (DI) water. This optimized composition of electrolyte solution provides the maximum number of protons for CO_2 reduction reaction. Here, 5% Nb-doped MoS_2 nanosheets showed an improved current density compared to pristine MoS_2 and Ta-doped MoS_2 (Figure 3C). The catalyst displayed faradaic efficiencies oscillating from 12% to 82% towards CO formation in the potential range of -0.8 ± 0.16 V (Figure 3D). The formation rates for CO and H_2 at 0.8 V were 2.23×10^{-9} mol min^{-1} and 1.98×10^{-9} mol min^{-1}, respectively. As a result, Nb-MoS_2 nanosheets exhibited an excellent catalytic activity in terms of turnover frequency (TOF) at an overpotential of 50–150 mV. In-depth DFT calculations were also conducted to understand the CO_2 reduction pathway. The results showed that Mo edges of pure MoS_2 preferably form an *COOH intermediate at lower overpotential. Moreover, Nb atoms help to reduce the binding strength among Mo and CO, thereby minimizing onset potential to produce CO via formation of *CO and *COOH intermediates. These findings revealed that Nb-doped MoS_2 promotes faster desorption of CO compared to pristine MoS_2. Furthermore, DFT calculations revealed that a low concentration of Nb-doping selectively reduced CO_2 to CO. However, an increased Nb concentration over 5% showed a negative effect on CO_2 reduction performance because of the enlarged work function of $Mo_{1-x}Nb_xS_2$ composite. Therefore, an appropriate amount of metal doping to a catalyst can significantly influence electronic properties that may further intensify the overall catalytic performance. MoS_2 is a well-known catalyst for hydrogen evolution due to its unique structural characteristics where S atoms can make a strong bond with H^+ in the electrolyte solution [76–78]. Therefore, a smaller number of S atoms are available for the CO_2 reduction reaction. Addressing the issue, Yu and coworkers employed a structure-directing approach and fabricated 3D TiO_2@MoS_2 to make bonding between the unsaturated S atom and Ti metal, consequently making a large number of Mo atoms available for CO_2 reduction reaction [76]. The porous nanosheets of TiO_2 acted as a CO_2 adsorbent due to high surface area and abundant active sites (Figure 4A). Bonding between Ti and S atoms improved the electronic and adsorption properties of MoS_2 (Figure 4B showing Raman spectra of Ti-S band). Here, the electrolyte solution played an important role in product selectivity. The N_2-saturated solution led to hydrogen evolution, whereas current density was increased towards CO formation in the CO_2-saturated solution. Faradic efficiency of ≈2.8% towards CO formation was observed at the potential of −0.21 V, while at a more negative potential it reached up to 85% (Figure 4C). The catalyst showed excellent stability over 1000 cycles which revealed its superiority (Figure 4D). Interestingly, long-term stability over 14 h was observed at a steady potential of −0.70 V.

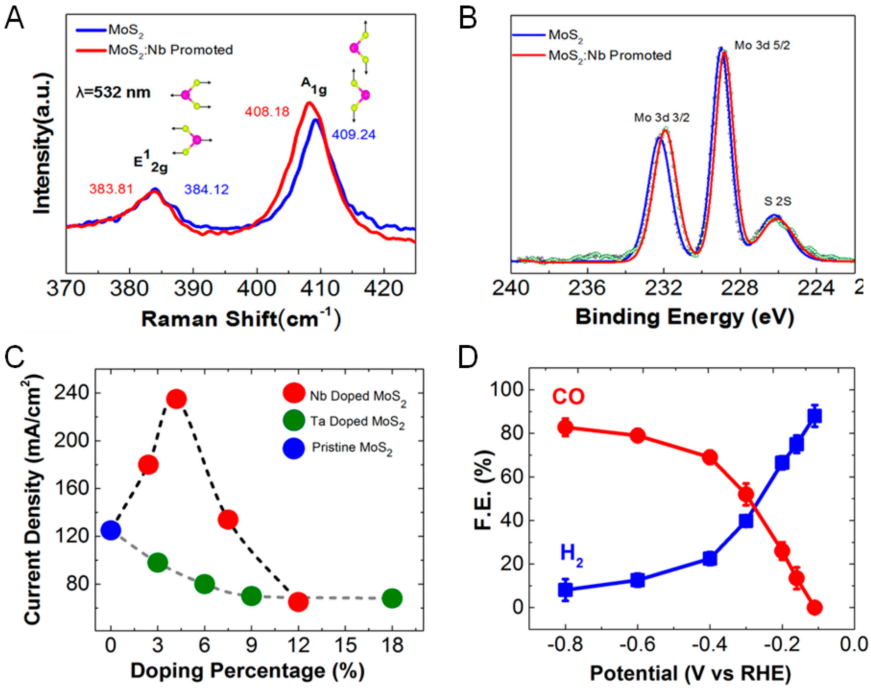

Figure 3. (**A**) Raman spectra and (**B**) XPS analyses of pristine MoS_2 and MoS_2: Nb; (**C**) current densities of different samples with respect to doping percentage, and (**D**) faradaic efficiencies (FE) of CO and H_2 formation at different applied potentials. Reprinted with permission from [57].

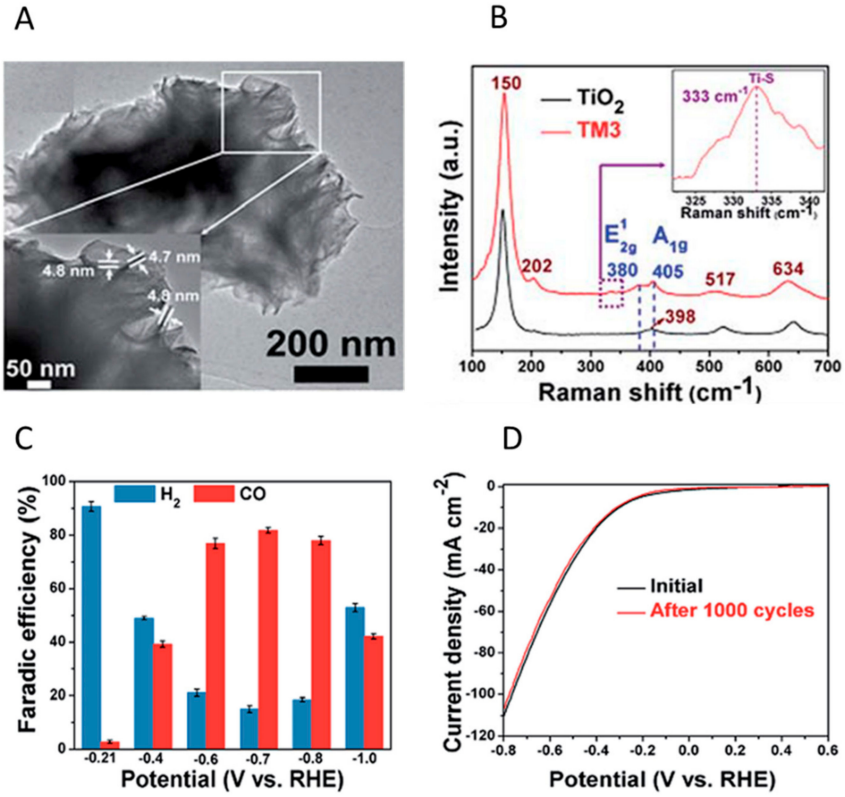

Figure 4. (**A**) TEM image showing edges inset; (**B**) Raman spectra; (**C**) Faradic efficiencies at applied potentials for CO and H_2 formation; and (**D**) Linear sweep voltammetry (LSV) curves showing current density at initial and after 1000 CV scans, for optimized 3D TiO_2@MoS_2. Reprinted with permission from [76].

3.2. 2D Graphene

Graphene has been playing a significant role in many advanced applications because of its high chemical stability, superior electronic and thermal properties, and high specific surface area [79]. Typically, pristine graphene is inactive towards electrocatalysis because of its ineffectiveness towards CO_2 activation. This allows a greater extent of freedom for surface modifications to tune the catalytic properties. The graphene templates, graphene oxide (GO), and reduced graphene oxide (RGO) have been largely employed for catalytic applications [80–83]. The metal and non-metal doping and composite formation with other semiconductors have been exercised to improve the catalytic performance of graphene. To date, metals like Cu, Ni, Au, and Co have been successfully used as dopants/co-catalyst [84]. Organometallic complexes and metal-organic frameworks (MOFs) have also been tried with graphene for CO_2 reduction [85,86]. Heteroatom doping (such as by nitrogen, boron, and sulfur) to graphene can effectively improve the CO_2 adsorption [87]. These heteroatoms act as reaction centers for CO_2 reduction and improve the catalytic activity [88,89]. For example, pyridinic N in the N-doped graphene possesses a lower free energy threshold to produce the COOH intermediate and selectively produce CO [90–93]. Additionally, the electrocatalyst comprising both metal and non-metal is significant for heterogeneous catalysis aiming towards product selectivity [94]. Su et al. synthesized Ni-nitrogenated-graphene (Ni-N-Gr) sheets for generation of CO from CO_2 [95]. The CO_2 reduction capability was examined by using cyclic voltammetry in the buffer solution and products were detected by GC-MS technique. At an optimized condition, Ni-N-Gr displayed the highest faradaic efficiency over 90% for CO production at −0.7 to −0.9 V. The Ni-N-Gr showed excellent catalytic performance with much higher activity than pristine Ni and N-Gr samples. To explore the significance of Ni in Ni-N-Gr composite, Cu-N-Gr was also tested as a control sample and results showed positive feedback towards the presence of Ni in composite. Further, the turnover frequencies of CO per electrochemically active Ni atom was up to 2700 h^{-1} at −0.7 V and 4600 h^{-1} at −0.8 V versus RHE. In another similar study, Ni^{2+} on nitrogen-doped graphene (Ni^{2+}@NG) was investigated for CO formation through electrocatalysis [88]. Previously, such types of catalysts were synthesized by utilizing the conservative pyrolysis technique (800–1000 °C) and acid leaching process, which are not so ecofriendly. Therefore, in this work the synthesis was carried out by employing a simple solution-chemistry approach which is convenient for large scale applicability. In this method, first N-doped graphene with an ultrathin nanosheet structure was synthesized by pyrolyzing a mixture of g-C_3N_4 and glucose. Then, immobilization of Ni^{2+} in N-doped graphene was carried out by reacting $Ni(NO_3)_2$ with N-doped graphene in the aqueous solution. The presence of Ni^{2+} ions and Ni valence state on N-doped graphene were confirmed by XPS and XANES spectra, respectively. The electrocatalyst produced CO with the faradaic efficiency of 92% at −0.68 V versus RHE. In contrast, the efficiency of pristine N-doped graphene was below 60% at all potential capacities. Therefore, Ni^{2+} sites significantly facilitated the kinetics of CO_2 reduction. Furthermore, to understand the effects of other transition metals ion, metals such as Co^{2+} and Fe^{3+} were likewise restrained on N-doped graphene. All the catalysts showed almost 4–5 times higher activity than pristine N-doped graphene. The composite with Ni^{2+} showed the highest faradaic efficiency of 92% compared to that of Fe^{3+} (85%) and Co^{2+} (65%); see Figure 5A. The formation of CO occurred via the *COOH (* is surface sites) intermediate (Figure 5B). The quadruple-pyridinic configuration of N-doped graphene exhibited the maximum free energy barrier which protonates *COOH to form *CO.

In certain composites, stabilization of the single metal atom within the 2D nanostructure is crucial to prevent aggregation. To address the issue, Jeong et al. reported single-atom Ni activated on RGO sheets for CO formation which showed a faradaic efficiency of 97% at 0.8 V versus RHE [96]. The linkage between Ni atoms and GO was accomplished by using the tris(2-benzimidazolylmethyl)amine (NTB) ligand (Figure 6A). Firstly, Ni(NTB) complex was prepared. The NTB ligand makes a strong bond with GO via π–π interaction and Ni ions via ligation by forming Ni(NTB)-GO complex. A uniform distribution of Ni atoms on 2D-RGO sheets was confirmed by TEM analysis. XANES analysis was used to confirm that nickel was in Ni^{2+} state rather than Ni^0. In an inert condition, the catalysts

displayed moderate activity towards the H_2 at −0.71 V versus RHE. Significantly the current density was improved in CO_2-saturated electrolyte, reaching the onset potential of −5 mA cm^{-2} at −0.60 V versus RHE. The observed current density was almost double at −1.1 V versus RHE, which implies its superior activity compared to that of control samples (Figure 6B). Ni-N-RGO showed the maximum faradaic efficiency (97%) for CO formation at −0.8 V versus RHE (Figure 6C). The reactivity of Ni-N_4 active sites towards the intermediate formed in the reaction are responsible for such high catalytic performance. DFT study revealed that the proton interactions with active sites of Ni-N-RGO are unfavorable towards HER. Therefore, selectivity was observed towards CO_2 reduction rather than H_2 formation.

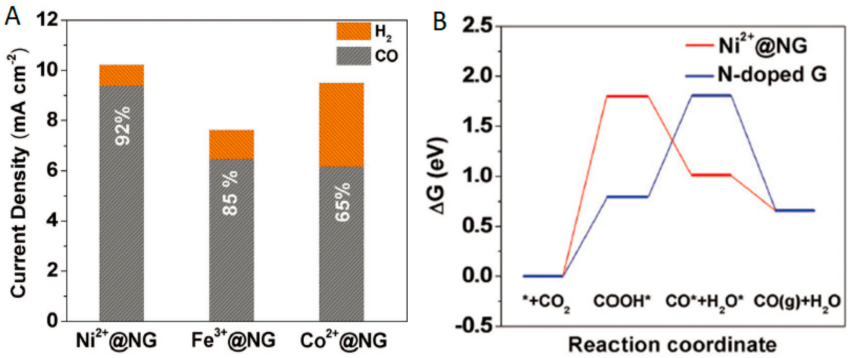

Figure 5. (**A**) The CO_2 performance for various transition metal ions restrained on N-graphene and (**B**) a free energy diagram showing the formation of CO via electrocatalytic CO_2 reduction. Reprinted with permission from [88].

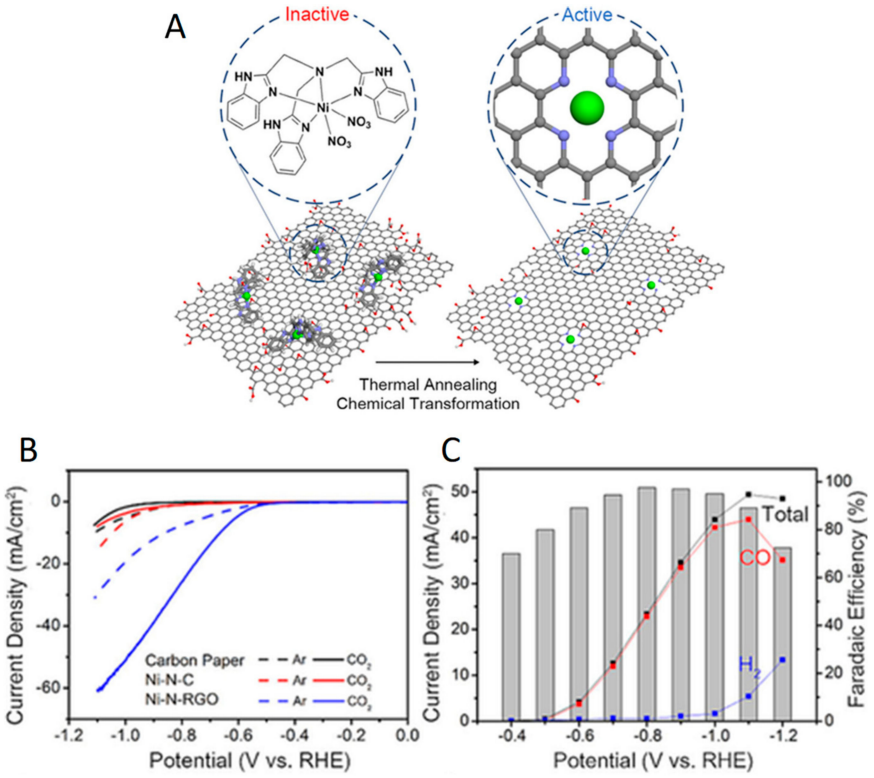

Figure 6. (**A**) Formation of Ni-N-RGO via chemical transformation of NTB adsorbed over RGO sheets; (**B**) LSV curves of different samples; and (**C**) faradaic efficiency of CO formation and current density versus applied potentials, reprinted with permission from [96].

Jiang and coworkers also demonstrated that graphene shells with embedded Ni atoms were active electrocatalysts for CO_2 reduction [97]. From DFT calculations it was observed that Ni atoms in the graphene layer can significantly lower the activation barrier of CO_2 molecule, which further weakens the binding with CO to form a facile product by lowering the proton reduction reaction. In this way, Ni-graphene electrocatalyst showed an excellent catalytic activity towards CO formation with a faradaic efficiency of 93.2% at current of 20 mA/mg. The turnover frequency (TOF) of 8 s^{-1} was observed for the active Ni center and a 454,000 cumulative turnover number (TON) was recorded below −0.7 V overpotential during 20 h of continuous electrolysis.

Jiang and coworkers reported more results with single Ni atoms emended in a graphene sheet [98]. Resulting catalysts endow CO selectivity over 90% of in aqueous solution, and the highest faradaic efficiency of CO (95%) was obtained at an overpotential of 550 mV. Specifically, Ni single atomic sites present in graphene were responsible for high selectivity of CO with 90% of faradaic efficiency over the stability of 20 h. Further, CO formation current, more than 200 mA (50 mA cm^{-2}) under a faradaic efficiency of 97%, was established by using a 4 cm^2 anion membrane electrode setup. Other transition metals, including Co, Fe, and Mn, were also dispersed on a graphene layer and it was observed that the reaction pathway changes with change in transition metals, specifically hydrogen was produced in the presence of Co. DFT studies revealed that for the Ni single atoms, compared to Co atoms, the weaker binding of CO and higher barrier for hydrogen evolution reaction accounted for the superior CO_2 reduction towards selective formation of CO.

The stability of the oxidation state among metals is very crucial for catalytic reactions. Copper is proven as one of the best and inexpensive catalysts for CO_2 reduction reaction. Karapinar et al. reported highly active, single-site Cu-N-C for electroreduction of CO_2 [99]. They found that during the catalytic process, isolated copper sites converted into metallic copper, which eventually act as active sites for the CO_2 reduction. Apart from nickel and copper, the iron-based catalysts are also considered as the superior and most active materials due to their chemical stability towards the CO_2 reduction under negative potential. The key parameter of this material is that Fe^{3+} can easily coordinate with N heteroatom supported on carbon and maintains its 3+ oxidation state throughout the electrocatalytic reaction [100]. Also, such Fe^{3+} sites can adsorb a greater number of CO_2 for electrocatalysis. Zhang and co-workers reported a hybrid composite of Fe/N-Graphene [101]. The electrocatalyst was fabricated by annealing the mixture of GO with iron chloride ($FeCl_3$) at 700–800 °C in an inert atmosphere, as shown in Figure 7A. The oxygen functional groups in GO adsorbed metal cations through the electrostatic interaction. Whereas, Fe atoms in N-graphene matrices created Fe-N_4 sites, which further acted as CO_2 activators. N dopant acted as an immobilizer among Fe atoms and the graphene surface through metal–nitrogen interaction. As a result, catalysts undergo selective CO_2 reduction towards CO formation with a faradaic efficiency of 80% at low potential of −0.60 V versus RHE. The catalyst was operated over 10 h at −0.60 V versus RHE to examine its long-term stability. The mechanism of CO_2 to CO conversion was studied by theoretical simulations. The formation of CO took place by sharing of two protons and two electrons via COOH* intermediate, as revealed in Figure 7. Here, substitution of nitrogen to graphene lowered the energy barrier of COOH* intermediate and facilitated the CO* formation.

Zhu and coworkers reported the superior catalytic activity of 94.2%, the faradaic efficiency for CO formation by employing 2D N-doped carbon nanorod arrays/ultrathin carbon nanosheet catalysts [102]. In the synthesis, aniline polymerization was carried out in the presence of carbon nanosheets and acid treatment, and resulting catalysts were obtained by pyrolysis. It was observed that the catalyst was proficient of retaining its activity for 30 h at a minimal onset overpotential of 97 mV. In the Tafel slope, a low value of 65 mV dec^{-1} specified a fast pre-equilibration process of transfer of one electron followed by a rate-determining step. DFT calculation suggests that the N pyridinic sites and 2D structure were responsible for lowering the free energy barriers of intermediates (*COOH and *CO) and boosting CO desorption to form CO. Therefore, these results showed an excellent catalytic activity among other reported doped carbon materials.

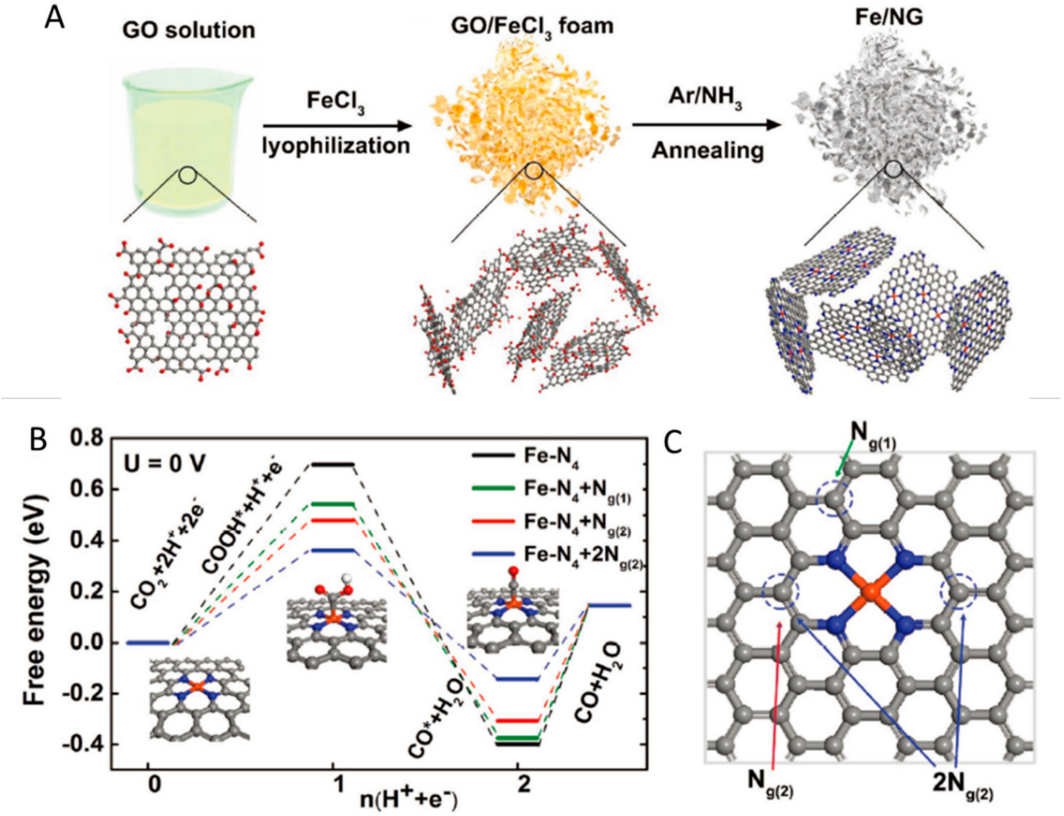

Figure 7. (**A**) The synthesis method of the Fe/NG catalyst; (**B**) free energy diagram showing mechanism of CO_2 reduction to CO; and (**C**) the structure for Fe-N_4 moieties on layered graphene showing nitrogen-substitution. Reprinted with permission from [97].

Apart from single metal atom insertion, the transition metal sulfides have also been tried with graphene. For example, silver sulfide (Ag_2S) possesses excellent physical, chemical, and thermal properties that are suitable for catalytic applications. Along those lines, Zeng et al. reported Ag_2S/N-S doped rGO hybrid for CO_2 reduction [103]. A hydrothermally synthesized, Ag_2S/N-S-doped rGO electrocatalyst was employed for CO_2 reduction toward CO. Here, CO, H_2, and CH_4 were obtained as products, while selectivity for CO was observed in the wide potential range of −1.08 to −0.58 V versus RHE. The catalyst manifested a current density of 470 μAcm^{-2} at −0.759 V versus RHE. An excellent catalytic activity owing to a faradaic efficiency of 87%, and long-term stability over 40 h, were achieved by the catalyst. The faradaic efficiency of this catalyst was enormously higher than pristine N-S-rGO (3.2%) and Ag_2S nanowires (41.7%) [104]. Significantly, an increase in current density was observed, as the potential was swept cathodically which specified the increase in CO_2 reduction kinetics in the system. In the CO formation mechanism, Ag ions bind with CO_2 molecule and generate a COOH intermediate by combining one proton and one electron. Afterwards, the intermediate (COOH) further reacts with a second proton and electron pair to form CO. The high surface area of rGO maximized the reactive sites for CO_2 molecule and N-S doping eventually enhanced the electrical conductivity of rGO.

Pitch derived 2D N-doped porous carbon nanosheets, which are similar to graphene, were also found to be a superior catalyst for selective CO_2 reduction with high stability [105]. For synthesis, the authors used a NH_3 etching strategy using NaCl template. NH_3 etching increases the catalyst's surface area by creating nanopores, and further, helping to insert nitrogen atoms into a carbon framework. Resulting catalysts showed high catalytic performance with 84% of faradaic efficiency at an overpotential of −0.49 V and a negligible onset overpotential of −0.9 V for CO production. Such excellent catalytic behavior was due to presence of nanoporous 2D architecture and the high content of pyridinic N active sites which favored fast charge transfer, and high CO_2 adsorption. DFT

studies confirmed that the pyridinic N sites favorably bind with COOH* intermediates and further facilitate catalytic reduction.

3.3. 2D Tungsten TMDCs

Tungsten is an emerging candidate for sustainable energy applications due to its low price, non-toxicity, and large atomic size compared with other TMDCs [106–111]. Due to its exciting electronic properties, tungsten dichalcogenides act as a catalytic site for electrochemical CO_2 reduction reactions. Also, tungsten dichalcogenides have the anisotropic properties of its basal and edge plane; therefore, most of the catalytic reactions occur on the edge sites [112]. These limited catalytic sites can be increased by transition metal doping [113]. In this regard, Asadi et al. fabricated the WSe_2 nanoflakes (NFs) by a chemical vapor transport growth and exfoliation technique [114]. They found that the CO_2 reduction activity of TMDCs in 50% EMIM-BF_4 with water was much higher compared to other TMDCs and Ag NPs. According to work functions estimation, the trend of monolayer TMDCs showed activity in the order WSe_2 < $MoSe_2$ < WS_2 < MoS_2 (Figure 8A). WSe_2 NFs had the lowest work function of those comprised of monolayered TMDCs. Also, electrochemical impedance spectroscopy (EIS) outcomes were matched with the work function trend (Figure 8B).

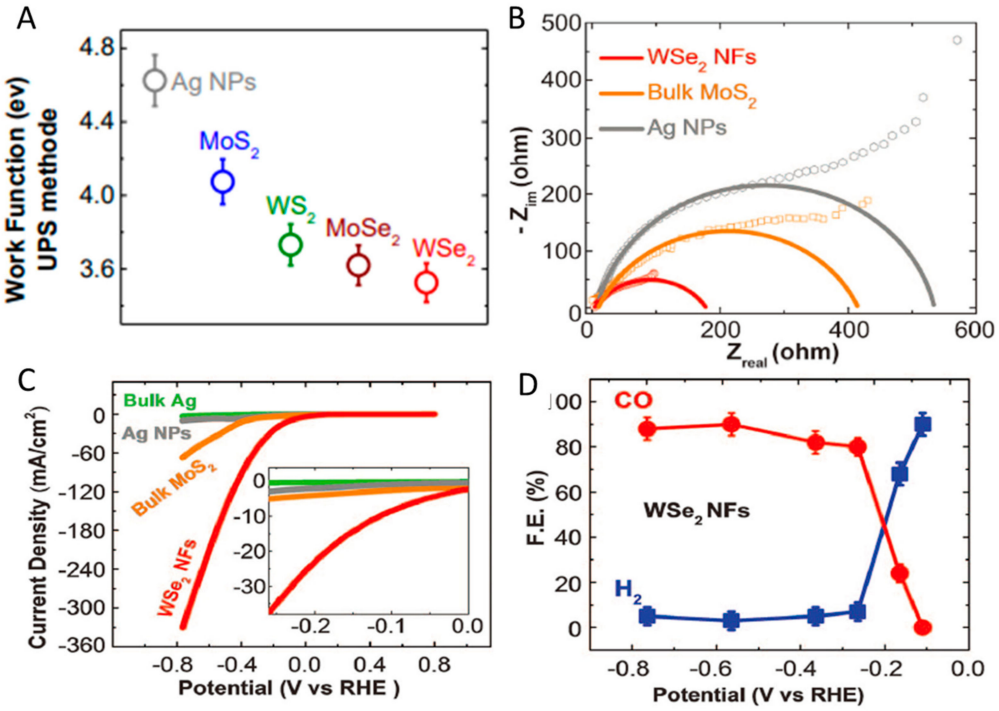

Figure 8. (**A**) Work functions of transition metal dichalcogenides (TMDCs) and Ag NPs; (**B**) CO_2 reduction electrochemical impedance spectroscopy (EIS); (**C**) Cyclic voltammetry curves and (**D**) faradaic efficiency curves by applied potential. Reprinted with permission from [114].

Charge transfer resistance (R_{ct}) is an important kinetic factor for the electrochemical rate constant. Charge transmission resistance of WSe_2 NFs (≈180 Ω) was lower than MoS_2 and Ag nanoparticles (Figure 8B) [114]. Therefore, WSe_2 possesses a fast electron transfer property which eventually affects the CO_2 reduction reaction. Experiments were performed in an electrolyte solution of 50% EMIM-BF_4, 50% water. It was found that WSe_2 NFs displayed a 18.95 mA cm^{-2} current density for CO at a minimal potential of 54 mV (Figure 8C,D). Here, $EMIM^+$ ion in the ionic liquid acted as a transporter of CO_2 to the catalyst surface. Also, the CO intermediate was more stable on the metallic edges of WSe_2 NFs, suggesting the possibility of CO formation after CO_2 reduction. Therefore, such systems owing to high catalytic performance operating at low overpotentials have the disruptive potential to solve the current obstacles of CO_2 reduction technology.

3.4. 2D InSe

Among various 2D materials, InSe is also considered as an emerging electrocatalyst. Although InSe is not a transition metal chalcogenide, we intentionally added this section to our study. Recently, the theoretical study about InSe was carried out by Jiang et al., which demonstrated its potential for CO_2 reduction [115]. The single metal (e.g., Rh, Mn, Cu, Zn, and Cr) was embedded in a 2D InSe substrate and catalytic reactivity towards CO, HCOOH, H_2, and CH_4 were studied. They showed that InSe systems with Rh, Mn, and Cu metals obeyed the linear scaling relationships among adsorption energies of intermediates, such as *CO and *COOH. However, the relationship broke down for system containing Zn and Cr metals. Such an interesting feature of 2D InSe offers a reliable method for the experimental usage, and in turn, the product selectivity. The Zn@2D InSe system effectively produces CO with limiting the potential of −0.78 V because it is situated on the scaling line among *COOH and *CO. Its lowered desorption energy (0.14 eV) executes selectivity towards CO. Therefore, such theoretical studies enrich the understanding of 2D systems for electrocatalytic applications.

The summary of various 2D nanomaterials for electrochemical CO_2 reduction is displayed in Table 2.

Table 2. The summary of various 2D nanomaterials for electrochemical CO_2 reduction. Details included reactor type, example of catalysts, current density, onset potential, over potential, and the main product of CO_2 reduction with faradaic efficiency and stability.

No	Catalyst	Current Density (versus Applied Potential)	Onset Potential (V) or Overpotential (versus RHE)	CO Faradaic Efficacy (FE% versus RHE)	Stability (versus RHE)	Reactor (Type, Volume), Electrolyte	Ref, Year
1	MoS_2	65 mA cm^{-2}	−0.764 V	98% @ −0.764 V	10 h @ −0.764 V	Two-compartment three-electrode electrochemical cell in Ionic liquid, 96:4 mol% water:EMI-BF_4	[74], 2014
2	Metal doped MoS_2			Theoretical study			[56], 2016
3	MoS_2 and $MoSe_2$			Theoretical study			[75], 2014
4	Nb-MoS_2	237 mA cm^{-2}	31 mV @ −0.8 V	82% @ −0.8 V	10 h @−0.8 V	Two-compartment three-electrode electrochemical cell, Ionic liquid, CO_2 saturated50:50 vol% EMIM-BF_3:water	[57], 2016
5	3D TiO_2@MoS_2	68 mA cm^{-2}	100 mV @ −0.7 V	85% @ −0.70 V	14 h @ −0.70 V	Three-electrode system, CO_2-saturated 0.1 M Potassium bicarbonate	[76], 2018
6	Nickel-nitrogen-modified graphene (Ni-N-Gr)	≈1.45 mA cm^{-2}	−0.5 V	90% @ −0.7 to −0.9 V	5 h @ −0.65 V	CO_2-saturated 0.1 M Potassium bicarbonate	[95], 2016
7	Ni^{2+} on N-doped graphene (Ni^{2+}@NG)	10.2 mA cm^{-2}	≈−0.40 V	92% @ −0.68 V	20 h (≈2.85 → ≈−2.44 mA cm^2) @ −0.58 V	Three-electrode system, CO_2-saturated 0.5 M Potassium bicarbonate	[88], 2019
8	Atomic iron dispersed on N-doped graphene (Fe/NG)	2.6 mA cm^{-2}	− 0.28 V	80% @ −0.60 V	10 h @ −0.60 V	CO_2-saturated 0.1 M Potassium bicarbonate solution	[101], 2018
9	Nickel- and nitrogen-doped reduced graphene oxide (Ni-N-rGO)	5 mA cm^{-2}	−0.60 V	97%@ −0.8V	-	Two-compartment electrochemical cell (Nafion 117 membrane) CO_2-saturated 0.5 M Potassium bicarbonate	[96], 2018
10	Nickel-N-doped graphene shell (Ni-N-GS)	4 mA cm^{-2}	0.7 V	93.2% @ 0.7 V	20 h @ 0.7 V	A homemade Teflon H-cell, CO_2-saturated 0.5 M Potassium bicarbonate	[97], 2017
11	Ni single atoms in graphene nanosheets (Ni-G)	50 mA cm^{-2}	480 mV	90% @ −0.87 V	20 h @ 0.64 V	A homemade Teflon H-cell, CO_2-saturated 0.5 M Potassium bicarbonate	[98], 2018
12	1D/2D N-doped carbon nanorod arrays/ultrathin carbon nanosheets	3.78 mA cm^{-2}	97 mV, @ −0.45 V	94.2% @ −0.45 V	30 h, @ −0.45 V	A homemade three-electrode system, CO_2-saturated 0.5 M Potassium bicarbonate	[102], 2019
13	Ag_2S/N-S-doped rGO	70 μA cm^{-2}	−0.34 V	87.4% @ −0.76V	40 h @ −0.759 V	Double-chamber electrochemical cell with a Nafion 117 membrane 0.1 M Potassium bicarbonate	[103], 2018
14	2D N-doped porous carbon nanosheets	1.15 mA cm^{-2}	−0.19 V	84% @ −0.49 V	8 h @ −0.60 V	Ar or CO_2-saturated 0.1 M Potassium bicarbonate	[105], 2018
15	WSe_2 nanoflakes (NFs)	18.95 mA cm^{-2}	54 mV	24% @ 54 mV	27 h @ −0.364 V	Three-electrode two- compartment cell ionic liquid set-up (50% EMIM-water)	[114], 2016
16	Metal@2D InSe			Theoretical study			[115], 2019

4. Conclusions

In the field of electrocatalytic CO_2 reduction, recent studies were mainly concentrated on the design of various types of efficient catalysts. A variety of tailored 2D nanostructures were fabricated by researchers with the rational design of experimental procedures. In particular, metal and non-metal doped 2D templates could be highly efficient and stable catalysts. In this study, we have briefly reviewed the recent developments in selective electrochemical CO_2 reduction to CO using various 2D nanostructures. The foremost goal of this study was to introduce the fundamentals and different synthetic strategies of 2D materials. The high surface area of 2D nanostructure encourages CO_2 adsorption, and the presence of edge sites/dopants helps to generate reactive sites for CO_2 reduction. Besides, single atom doped 2D structures hold great potential for electrocatalytic CO_2 reduction, since they have been shown to have high faradaic efficiency along with CO selectivity. While highlighting the different fabrication methods, we have also paid considerable attention to the theoretical studies because theoretical simulations are of equal importance to understand the reactivity, product selectivity, and mechanism of CO_2 reduction pathway. Although several noteworthy successes in CO_2 reduction have been achieved by 2D based nanostructures, further efforts are required for large scale applications. Additionally, more focus should be given toward improving upon the green, scalable, and sustainable electrocatalyst fabrications, which is becoming a crucial factor for realistic industrial applications. Apart from that, CO_2 transformation into higher hydrocarbon products such as ethane, ethanol, or ethylene is also of similar importance, and has a great challenge ahead due to the low efficiency of the existing catalysts. Copper-based catalysts have been proven to be superior materials for generating higher hydrocarbons, including C_2 and C_3 products. However, we believe that the interesting surface, electronic, and structural properties of 2D materials could also be significant in higher hydrocarbon production in the near future.

Author Contributions: S.-I.I. conceptualized and edited the manuscript; C.B.H., H.K., J.L., S.S., and C.E. wrote the manuscript. All authors have read and agreed to the published version of the manuscript.

Funding: The authors thankfully acknowledge the support of the Ministry of Science and ICT (2017R1E1A1A01074890 and 2017M2A2A6A01070912). This research was also supported by the Technology Development Program to Solve Climate Changes of the National Research Foundation (NRF) funded by the Ministry of Science and ICT (2015M1A2A2074670) and by Flux Photon Corporation.

Conflicts of Interest: The authors declare no conflict of interest.

References

1. Zhou, H.; Li, P.; Liu, J.; Chen, Z.; Liu, L.; Dontsova, D.; Yan, R.; Fan, T.; Zhang, D.; Ye, J. Biomimetic polymeric semiconductor based hybrid nanosystems for artificial photosynthesis towards solar fuels generation via CO_2 reduction. *Nano Energy* **2016**, *25*, 128–135. [CrossRef]
2. Sorcar, S.; Thompson, J.; Hwang, Y.; Park, Y.H.; Majima, T.; Grimes, C.A.; Durrant, J.R.; In, S.-I. High-rate solar-light photoconversion of CO_2 to fuel: Controllable transformation from C_1 to C_2 products. *Energy Environ. Sci.* **2018**, *11*, 3183–3193. [CrossRef]
3. Marszewski, M.; Cao, S.; Yu, J.; Jaroniec, M. Semiconductor-based photocatalytic CO_2 conversion. *Mater. Horizons* **2015**, *2*, 261–278. [CrossRef]
4. Bushuyev, O.S.; De Luna, P.; Dinh, C.T.; Tao, L.; Saur, G.; van de Lagemaat, J.; Kelley, S.O.; Sargent, E.H. What should we make with CO_2 and how can we make it? *Joule* **2018**, *2*, 825–832. [CrossRef]
5. Razzaq, A.; In, S.-I. TiO_2 Based Nanostructures for Photocatalytic CO_2 Conversion to Valuable Chemicals. *Micromachines* **2019**, *10*, 326. [CrossRef] [PubMed]
6. Thomas, J.M.; Harris, K.D.M. Some of tomorrow's catalysts for processing renewable and non-renewable feedstocks, diminishing anthropogenic carbon dioxide and increasing the production of energy. *Energy Environ. Sci.* **2016**, *9*, 687–708. [CrossRef]
7. Hiragond, C.; Ali, S.; Sorcar, S.; In, S.-I. Hierarchical Nanostructured Photocatalysts for CO_2 Photoreduction. *Catalysts* **2019**, *9*, 370. [CrossRef]

8. Ali, S.; Razzaq, A.; In, S.-I. Development of graphene based photocatalysts for CO_2 reduction to C_1 chemicals: A brief overview. *Catal. Today* **2019**, *335*, 39–54. [CrossRef]
9. Qiao, J.; Liu, Y.; Hong, F.; Zhang, J. A review of catalysts for the electroreduction of carbon dioxide to produce low-carbon fuels. *Chem. Soc. Rev.* **2014**, *43*, 631–675. [CrossRef]
10. Kondratenko, E.V.; Mul, G.; Baltrusaitis, J.; Larrazábal, G.O.; Pérez-Ramírez, J. Status and perspectives of CO_2 conversion into fuels and chemicals by catalytic, photocatalytic and electrocatalytic processes. *Energy Environ. Sci.* **2013**, *6*, 3112–3135. [CrossRef]
11. Taheri Najafabadi, A. CO_2 chemical conversion to useful products: An engineering insight to the latest advances toward sustainability. *Int. J. Energy Res.* **2013**, *37*, 485–499. [CrossRef]
12. Lorentzou, S.; Karagiannakis, G.; Pagkoura, C.; Zygogianni, A.; Konstandopoulos, A.G. Thermochemical CO_2 and CO_2/H_2O splitting over $NiFe_2O_4$ for solar fuels synthesis. *Energy Procedia* **2014**, *49*, 1999–2008. [CrossRef]
13. Chueh, W.C.; Falter, C.; Abbott, M.; Scipio, D.; Furler, P.; Haile, S.M.; Steinfeld, A. High-flux solar-driven thermochemical dissociation of CO_2 and H_2O using nonstoichiometric ceria. *Science* **2010**, *330*, 1797–1801. [CrossRef] [PubMed]
14. Sorcar, S.; Hwang, Y.; Grimes, C.A.; In, S.-I. Highly enhanced and stable activity of defect-induced titania nanoparticles for solar light-driven CO_2 reduction into CH_4. *Mater. Today* **2017**, *20*, 507–515. [CrossRef]
15. Sorcar, S.; Hwang, Y.; Lee, J.; Kim, H.; Grimes, K.M.; Grimes, C.A.; Jung, J.-W.; Cho, C.-H.; Majima, T.; Hoffmann, M.R.; et al. CO_2, water, and sunlight to hydrocarbon fuels: A sustained sunlight to fuel (Joule-to-Joule) photoconversion efficiency of 1%. *Energy Environ. Sci.* **2019**, *12*, 2685–2696. [CrossRef]
16. Razzaq, A.; Sinhamahapatra, A.; Kang, T.-H.; Grimes, C.A.; Yu, J.-S.; In, S.-I. Efficient solar light photoreduction of CO_2 to hydrocarbon fuels via magnesiothermally reduced TiO_2 photocatalyst. *Appl. Catal. B Environ.* **2017**, *215*, 28–35. [CrossRef]
17. Zubair, M.; Kim, H.; Razzaq, A.; Grimes, C.A.; In, S.-I. Solar spectrum photocatalytic conversion of CO_2 to CH_4 utilizing TiO_2 nanotube arrays embedded with graphene quantum dots. *J. CO2 Util.* **2018**, *26*, 70–79. [CrossRef]
18. Ali, S.; Flores, M.C.; Razzaq, A.; Sorcar, S.; Hiragond, C.B.; Kim, H.R.; Park, Y.H.; Hwang, Y.; Kim, H.S.; Kim, H.; et al. Gas Phase Photocatalytic CO_2 Reduction,"A Brief Overview for Benchmarking". *Catalysts* **2019**, *9*, 727. [CrossRef]
19. Kim, H.R.; Razzaq, A.; Grimes, C.A.; In, S.-I. Heterojunction pnp Cu_2O/S-TiO_2/CuO: Synthesis and application to photocatalytic conversion of CO_2 to methane. *J. CO2 Util.* **2017**, *20*, 91–96. [CrossRef]
20. Kim, K.; Razzaq, A.; Sorcar, S.; Park, Y.; Grimes, C.A.; In, S.-I. Hybrid mesoporous Cu_2 $ZnSnS_4$ (CZTS)–TiO_2 photocatalyst for efficient photocatalytic conversion of CO_2 into CH_4 under solar irradiation. *RSC Adv.* **2016**, *6*, 38964–38971. [CrossRef]
21. Park, S.-M.; Razzaq, A.; Park, Y.H.; Sorcar, S.; Park, Y.; Grimes, C.A.; In, S.-I. Hybrid Cu_xO–TiO_2 Heterostructured Composites for Photocatalytic CO_2 Reduction into Methane Using Solar Irradiation: Sunlight into Fuel. *ACS Omega* **2016**, *1*, 868–875. [CrossRef] [PubMed]
22. Ganesh, I. Electrochemical conversion of carbon dioxide into renewable fuel chemicals–The role of nanomaterials and the commercialization. *Renew. Sustain. Energy Rev.* **2016**, *59*, 1269–1297. [CrossRef]
23. Benson, E.E.; Kubiak, C.P.; Sathrum, A.J.; Smieja, J.M. Electrocatalytic and homogeneous approaches to conversion of CO_2 to liquid fuels. *Chem. Soc. Rev.* **2009**, *38*, 89–99. [CrossRef] [PubMed]
24. Bhugun, I.; Lexa, D.; Savéant, J.-M. Catalysis of the electrochemical reduction of carbon dioxide by iron (0) porphyrins: Synergystic effect of weak Brönsted acids. *J. Am. Chem. Soc.* **1996**, *118*, 1769–1776. [CrossRef]
25. Shi, J.; Jiang, Y.; Jiang, Z.; Wang, X.; Wang, X.; Zhang, S.; Han, P.; Yang, C. Enzymatic conversion of carbon dioxide. *Chem. Soc. Rev.* **2015**, *44*, 5981–6000. [CrossRef]
26. Olajire, A.A. A review of mineral carbonation technology in sequestration of CO_2. *J. Pet. Sci. Eng.* **2013**, *109*, 364–392. [CrossRef]
27. Chu, S.; Majumdar, A. Opportunities and challenges for a sustainable energy future. *Nature* **2012**, *488*, 294. [CrossRef]
28. Yu, F.; Wei, P.; Yang, Y.; Chen, Y.; Guo, L.; Peng, Z. Material design at nano and atomic scale for electrocatalytic CO_2 reduction. *Nano Mater. Sci.* **2019**, *1*, 60–69. [CrossRef]

29. Khezri, B.; Fisher, A.C.; Pumera, M. CO_2 reduction: The quest for electrocatalytic materials. *J. Mater. Chem. A* **2017**, *5*, 8230–8246. [CrossRef]
30. Zhang, W.; Hu, Y.; Ma, L.; Zhu, G.; Wang, Y.; Xue, X.; Chen, R.; Yang, S.; Jin, Z. Progress and perspective of electrocatalytic CO_2 reduction for renewable carbonaceous fuels and chemicals. *Adv. Sci.* **2018**, *5*(5), 1700275. [CrossRef]
31. Wei, J.; Ge, Q.; Yao, R.; Wen, Z.; Fang, C.; Guo, L.; Xu, H.; Sun, J. Directly converting CO_2 into a gasoline fuel. *Nat. Commun.* **2017**, *8*, 825–832. [CrossRef] [PubMed]
32. Li, W.; Wang, H.; Jiang, X.; Zhu, J.; Liu, Z.; Guo, X.; Song, C. A short review of recent advances in CO_2 hydrogenation to hydrocarbons over heterogeneous catalysts. *RSC Adv.* **2018**, *8*, 7651–7669. [CrossRef]
33. Kuhl, K.P.; Hatsukade, T.; Cave, E.R.; Abram, D.N.; Kibsgaard, J.; Jaramillo, T.F. Electrocatalytic conversion of carbon dioxide to methane and methanol on transition metal surfaces. *J. Am. Chem. Soc.* **2014**, *136*, 14107–14113. [CrossRef] [PubMed]
34. Rogers, C.; Perkins, W.S.; Veber, G.; Williams, T.E.; Cloke, R.R.; Fischer, F.R. Synergistic enhancement of electrocatalytic CO_2 reduction with gold nanoparticles embedded in functional graphene nanoribbon composite electrodes. *J. Am. Chem. Soc.* **2017**, *139*, 4052–4061. [CrossRef]
35. Hernández, S.; Farkhondehfal, M.A.; Sastre, F.; Makkee, M.; Saracco, G.; Russo, N. Syngas production from electrochemical reduction of CO_2: Current status and prospective implementation. *Green Chem.* **2017**, *19*, 2326–2346. [CrossRef]
36. Zhu, W.; Michalsky, R.; Metin, O.; Lv, H.; Guo, S.; Wright, C.J.; Sun, X.; Peterson, A.A.; Sun, S. Monodisperse Au nanoparticles for selective electrocatalytic reduction of CO_2 to CO. *J. Am. Chem. Soc.* **2013**, *135*, 16833–16836. [CrossRef]
37. Zhou, W.; Cheng, K.; Kang, J.; Zhou, C.; Subramanian, V.; Zhang, Q.; Wang, Y. New horizon in C_1 chemistry: Breaking the selectivity limitation in transformation of syngas and hydrogenation of CO_2 into hydrocarbon chemicals and fuels. *Chem. Soc. Rev.* **2019**, *48*, 3193–3228. [CrossRef]
38. Ju, W.; Bagger, A.; Hao, G.-P.; Varela, A.S.; Sinev, I.; Bon, V.; Cuenya, B.R.; Kaskel, S.; Rossmeisl, J.; Strasser, P. Understanding activity and selectivity of metal-nitrogen-doped carbon catalysts for electrochemical reduction of CO_2. *Nat. Commun.* **2017**, *8*, 944. [CrossRef]
39. Dai, L.; Qin, Q.; Wang, P.; Zhao, X.; Hu, C.; Liu, P.; Qin, R.; Chen, M.; Ou, D.; Xu, C. Ultrastable atomic copper nanosheets for selective electrochemical reduction of carbon dioxide. *Sci. Adv.* **2017**, *3*, e1701069. [CrossRef]
40. Rasul, S.; Pugnant, A.; Xiang, H.; Fontmorin, J.-M.; Eileen, H.Y. Low cost and efficient alloy electrocatalysts for CO_2 reduction to formate. *J. CO2 Util.* **2019**, *32*, 1–10. [CrossRef]
41. Qiu, J.-P.; Tong, Y.-W.; Zhao, D.-M.; He, Z.-Q.; Chen, J.-M.; Song, S. Electrochemical reduction of CO_2 to methanol at TiO_2 nanotube electrodes. *Acta Phys. Chim. Sin.* **2017**, *33*, 1411–1420.
42. Gao, D.; Zhang, Y.; Zhou, Z.; Cai, F.; Zhao, X.; Huang, W.; Li, Y.; Zhu, J.; Liu, P.; Yang, F. Enhancing CO_2 electroreduction with the metal–oxide interface. *J. Am. Chem. Soc.* **2017**, *139*, 5652–5655. [CrossRef] [PubMed]
43. Lin, S.; Diercks, C.S.; Zhang, Y.-B.; Kornienko, N.; Nichols, E.M.; Zhao, Y.; Paris, A.R.; Kim, D.; Yang, P.; Yaghi, O.M. Covalent organic frameworks comprising cobalt porphyrins for catalytic CO_2 reduction in water. *Science* **2015**, *349*, 1208–1213. [CrossRef] [PubMed]
44. Li, N.; Chen, X.; Ong, W.-J.; MacFarlane, D.R.; Zhao, X.; Cheetham, A.K.; Sun, C. Understanding of electrochemical mechanisms for CO_2 capture and conversion into hydrocarbon fuels in transition-metal carbides (MXenes). *ACS Nano* **2017**, *11*, 10825–10833. [CrossRef]
45. Back, S.; Jung, Y. TiC-and TiN-supported single-atom catalysts for dramatic improvements in CO_2 electrochemical reduction to CH_4. *ACS Energy Lett.* **2017**, *2*, 969–975. [CrossRef]
46. Wang, Y.; Hou, P.; Wang, Z.; Kang, P. Zinc Imidazolate Metal–Organic Frameworks (ZIF-8) for Electrochemical Reduction of CO_2 to CO. *ChemPhysChem* **2017**, *18*, 3142–3147. [CrossRef]
47. Dou, S.; Song, J.; Xi, S.; Du, Y.; Wang, J.; Huang, Z.; Xu, Z.J.; Wang, X. Boosting Electrochemical CO_2 Reduction on Metal–Organic Frameworks via Ligand Doping. *Angew. Chemie* **2019**, *131*, 4081–4085. [CrossRef]
48. Shao, P.; Yi, L.; Chen, S.; Zhou, T.; Zhang, J. Metal-organic frameworks for electrochemical reduction of carbon dioxide: The role of metal centers. *J. Energy Chem.* **2019**, *40*, 156–170. [CrossRef]
49. Hao, J.; Shi, W. Transition metal (Mo, Fe, Co, and Ni)-based catalysts for electrochemical CO_2 reduction. *Chin. J. Catal.* **2018**, *39*, 1157–1166. [CrossRef]

50. Tayyebi, E.; Hussain, J.; Abghoui, Y.; Skúlason, E. Trends of electrochemical CO_2 reduction reaction on transition metal oxide catalysts. *J. Phys. Chem. C* **2018**, *122*, 10078–10087. [CrossRef]
51. Qu, J.; Zhang, X.; Wang, Y.; Xie, C. Electrochemical reduction of CO_2 on RuO_2/TiO_2 nanotubes composite modified Pt electrode. *Electrochim. Acta* **2005**, *50*, 3576–3580. [CrossRef]
52. Karamad, M.; Hansen, H.A.; Rossmeisl, J.; Nørskov, J.K. Mechanistic pathway in the electrochemical reduction of CO_2 on RuO_2. *ACS Catal.* **2015**, *5*, 4075–4081. [CrossRef]
53. Zhang, H.; Cheng, H.-M.; Ye, P. 2D nanomaterials: Beyond graphene and transition metal dichalcogenides. *Chem. Soc. Rev.* **2018**, *47*, 6009–6012. [CrossRef] [PubMed]
54. Cai, X.; Luo, Y.; Liu, B.; Cheng, H.-M. Preparation of 2D material dispersions and their applications. *Chem. Soc. Rev.* **2018**, *47*, 6224–6266. [CrossRef]
55. Sun, Z.; Ma, T.; Tao, H.; Fan, Q.; Han, B. Fundamentals and challenges of electrochemical CO_2 reduction using two-dimensional materials. *Chem* **2017**, *3*, 560–587. [CrossRef]
56. Hong, X.; Chan, K.; Tsai, C.; Nørskov, J.K. How doped MoS_2 breaks transition-metal scaling relations for CO_2 electrochemical reduction. *ACS Catal.* **2016**, *6*, 4428–4437. [CrossRef]
57. Abbasi, P.; Asadi, M.; Liu, C.; Sharifi-Asl, S.; Sayahpour, B.; Behranginia, A.; Zapol, P.; Shahbazian-Yassar, R.; Curtiss, L.A.; Salehi-Khojin, A. Tailoring the edge structure of molybdenum disulfide toward electrocatalytic reduction of carbon dioxide. *ACS Nano* **2016**, *11*, 453–460. [CrossRef]
58. Indrakanti, V.P.; Kubicki, J.D.; Schobert, H.H. Photoinduced activation of CO_2 on Ti-based heterogeneous catalysts: Current state, chemical physics-based insights and outlook. *Energy Environ. Sci.* **2009**, *2*, 745–758. [CrossRef]
59. Habisreutinger, S.N.; Schmidt-Mende, L.; Stolarczyk, J.K. Photocatalytic reduction of CO_2 on TiO_2 and other semiconductors. *Angew. Chemie Int. Ed.* **2013**, *52*, 7372–7408. [CrossRef]
60. Wu, J.; Huang, Y.; Ye, W.; Li, Y. CO_2 reduction: From the electrochemical to photochemical approach. *Adv. Sci.* **2017**, *4*, 1700194. [CrossRef]
61. Yang, Y.; Lee, J.-W. Toward ideal carbon dioxide functionalization. *Chem. Sci.* **2019**, *10*, 3905–3926. [CrossRef] [PubMed]
62. Xie, S.; Zhang, Q.; Liu, G.; Wang, Y. Photocatalytic and photoelectrocatalytic reduction of CO_2 using heterogeneous catalysts with controlled nanostructures. *Chem. Commun.* **2016**, *52*, 35–59. [CrossRef] [PubMed]
63. Shehzad, N.; Tahir, M.; Johari, K.; Murugesan, T.; Hussain, M. A critical review on TiO_2 based photocatalytic CO_2 reduction system: Strategies to improve efficiency. *J. CO2 Util.* **2018**, *26*, 98–122. [CrossRef]
64. Hong, J.; Zhang, W.; Ren, J.; Xu, R. Photocatalytic reduction of CO_2: A brief review on product analysis and systematic methods. *Anal. Methods* **2013**, *5*, 1086–1097. [CrossRef]
65. Mori, K.; Yamashita, H.; Anpo, M. Photocatalytic reduction of CO_2 with H_2O on various titanium oxide photocatalysts. *Rsc Adv.* **2012**, *2*, 3165–3172. [CrossRef]
66. Liu, L.; Liu, C. Origin of the overpotentials for $HCOO^-$ and CO formation in the electroreduction of CO_2 on Cu (211): The reductive desorption processes decide. *Phys. Chem. Chem. Phys.* **2018**, *20*, 5756–5765. [CrossRef]
67. Peterson, A.A.; Abild-Pedersen, F.; Studt, F.; Rossmeisl, J.; Nørskov, J.K. How copper catalyzes the electroreduction of carbon dioxide into hydrocarbon fuels. *Energy Environ. Sci.* **2010**, *3*, 1311–1315. [CrossRef]
68. Tian, Z.; Priest, C.; Chen, L. Recent Progress in the Theoretical Investigation of Electrocatalytic Reduction of CO_2. *Adv. Theory Simul.* **2018**, *1*, 1800004. [CrossRef]
69. Elgrishi, N.; Chambers, M.B.; Fontecave, M. Turning it off! Disfavouring hydrogen evolution to enhance selectivity for CO production during homogeneous CO_2 reduction by cobalt–terpyridine complexes. *Chem. Sci.* **2015**, *6*, 2522–2531. [CrossRef]
70. Rongé, J.; Bosserez, T.; Martel, D.; Nervi, C.; Boarino, L.; Taulelle, F.; Decher, G.; Bordiga, S.; Martens, J.A. Monolithic cells for solar fuels. *Chem. Soc. Rev.* **2014**, *43*, 7963–7981. [CrossRef]
71. Costentin, C.; Passard, G.; Robert, M.; Savéant, J.-M. Ultraefficient homogeneous catalyst for the CO_2-to-CO electrochemical conversion. *Proc. Natl. Acad. Sci. USA* **2014**, *111*, 14990–14994. [CrossRef]
72. Albo, J.; Alvarez-Guerra, M.; Castaño, P.; Irabien, A. Towards the electrochemical conversion of carbon dioxide into methanol. *Green Chem.* **2015**, *17*, 2304–2324. [CrossRef]

73. König, M.; Vaes, J.; Klemm, E.; Pant, D. Solvents and Supporting Electrolytes in the Electrocatalytic Reduction of CO_2. *iScience* **2019**, *19*, 135. [CrossRef] [PubMed]
74. Asadi, M.; Kumar, B.; Behranginia, A.; Rosen, B.A.; Baskin, A.; Repnin, N.; Pisasale, D.; Phillips, P.; Zhu, W.; Haasch, R. Robust carbon dioxide reduction on molybdenum disulphide edges. *Nat. Commun.* **2014**, *5*, 4470. [CrossRef] [PubMed]
75. Chan, K.; Tsai, C.; Hansen, H.A.; Nørskov, J.K. Molybdenum sulfides and selenides as possible electrocatalysts for CO_2 reduction. *ChemCatChem* **2014**, *6*, 1899–1905. [CrossRef]
76. Yu, L.; Xie, Y.; Zhou, J.; Li, Y.; Yu, Y.; Ren, Z. Robust and selective electrochemical reduction of CO_2: The case of integrated 3DTiO_2@ MoS_2 architectures and Ti–S bonding effects. *J. Mater. Chem. A* **2018**, *6*, 4706–4713. [CrossRef]
77. Hinnemann, B.; Moses, P.G.; Bonde, J.; Jørgensen, K.P.; Nielsen, J.H.; Horch, S.; Chorkendorff, I.; Nørskov, J.K. Biomimetic hydrogen evolution: MoS_2 nanoparticles as catalyst for hydrogen evolution. *J. Am. Chem. Soc.* **2005**, *127*, 5308–5309. [CrossRef]
78. Xiang, Q.; Yu, J.; Jaroniec, M. Synergetic effect of MoS_2 and graphene as cocatalysts for enhanced photocatalytic H_2 production activity of TiO_2 nanoparticles. *J. Am. Chem. Soc.* **2012**, *134*, 6575–6578. [CrossRef]
79. Ma, T.; Fan, Q.; Li, X.; Qiu, J.; Wu, T.; Sun, Z. Graphene-based materials for electrochemical CO_2 reduction. *J. CO2 Util.* **2019**, *30*, 168–182. [CrossRef]
80. Hossain, M.N.; Wen, J.; Chen, A. Unique copper and reduced graphene oxide nanocomposite toward the efficient electrochemical reduction of carbon dioxide. *Sci. Rep.* **2017**, *7*, 3184. [CrossRef]
81. Zhang, Z.; Ahmad, F.; Zhao, W.; Yan, W.; Zhang, W.; Huang, H.; Ma, C.; Zeng, J. Enhanced Electrocatalytic Reduction of CO_2 via Chemical Coupling between Indium Oxide and Reduced Graphene Oxide. *Nano Lett.* **2019**, *19*, 4029–4034. [CrossRef] [PubMed]
82. Yuan, J.; Zhi, W.-Y.; Liu, L.; Yang, M.-P.; Wang, H.; Lu, J.-X. Electrochemical reduction of CO_2 at metal-free N-functionalized graphene oxide electrodes. *Electrochim. Acta* **2018**, *282*, 694–701. [CrossRef]
83. Zhao, Y.; Wang, C.; Liu, Y.; MacFarlane, D.R.; Wallace, G.G. Engineering surface amine modifiers of ultrasmall gold nanoparticles supported on reduced graphene oxide for improved electrochemical CO_2 reduction. *Adv. Energy Mater.* **2018**, *8*, 1801400. [CrossRef]
84. Liu, X.; Zhu, L.; Wang, H.; He, G.; Bian, Z. Catalysis performance comparison for electrochemical reduction of CO_2 on Pd–Cu/graphene catalyst. *RSC Adv.* **2016**, *6*, 38380–38387. [CrossRef]
85. Shen, J.; Kortlever, R.; Kas, R.; Birdja, Y.Y.; Diaz-Morales, O.; Kwon, Y.; Ledezma-Yanez, I.; Schouten, K.J.P.; Mul, G.; Koper, M.T.M. Electrocatalytic reduction of carbon dioxide to carbon monoxide and methane at an immobilized cobalt protoporphyrin. *Nat. Commun.* **2015**, *6*, 8177. [CrossRef] [PubMed]
86. Kornienko, N.; Zhao, Y.; Kley, C.S.; Zhu, C.; Kim, D.; Lin, S.; Chang, C.J.; Yaghi, O.M.; Yang, P. Metal–organic frameworks for electrocatalytic reduction of carbon dioxide. *J. Am. Chem. Soc.* **2015**, *137*, 14129–14135. [CrossRef]
87. Liu, T.; Ali, S.; Lian, Z.; Li, B.; Su, D.S. CO_2 electoreduction reaction on heteroatom-doped carbon cathode materials. *J. Mater. Chem. A* **2017**, *5*, 21596–21603. [CrossRef]
88. Bi, W.; Li, X.; You, R.; Chen, M.; Yuan, R.; Huang, W.; Wu, X.; Chu, W.; Wu, C.; Xie, Y. Surface immobilization of transition metal ions on nitrogen-doped graphene realizing high-efficient and selective CO_2 reduction. *Adv. Mater.* **2018**, *30*, 1706617. [CrossRef]
89. Cui, H.; Guo, Y.; Guo, L.; Wang, L.; Zhou, Z.; Peng, Z. Heteroatom-doped carbon materials and their composites as electrocatalysts for CO_2 reduction. *J. Mater. Chem. A* **2018**, *6*, 18782–18793. [CrossRef]
90. Li, W.; Seredych, M.; Rodríguez-Castellón, E.; Bandosz, T.J. Metal-free Nanoporous Carbon as a Catalyst for Electrochemical Reduction of CO_2 to CO and CH_4. *ChemSusChem* **2016**, *9*, 606–616. [CrossRef]
91. Liu, S.; Yang, H.; Huang, X.; Liu, L.; Cai, W.; Gao, J.; Li, X.; Zhang, T.; Huang, Y.; Liu, B. Identifying Active Sites of Nitrogen-Doped Carbon Materials for the CO_2 Reduction Reaction. *Adv. Funct. Mater.* **2018**, *28*, 1800499. [CrossRef]
92. Zou, X.; Liu, M.; Wu, J.; Ajayan, P.M.; Li, J.; Liu, B.; Yakobson, B.I. How nitrogen-doped graphene quantum dots catalyze electroreduction of CO_2 to hydrocarbons and oxygenates. *ACS Catal.* **2017**, *7*, 6245–6250. [CrossRef]
93. Wang, H.; Jia, J.; Song, P.; Wang, Q.; Li, D.; Min, S.; Qian, C.; Wang, L.; Li, Y.F.; Ma, C. Efficient Electrocatalytic Reduction of CO_2 by Nitrogen-Doped Nanoporous Carbon/Carbon Nanotube Membranes: A Step Towards the Electrochemical CO_2 Refinery. *Angew. Chemie Int. Ed.* **2017**, *56*, 7847–7852. [CrossRef] [PubMed]

94. Varela, A.S.; Ranjbar Sahraie, N.; Steinberg, J.; Ju, W.; Oh, H.; Strasser, P. Metal-doped nitrogenated carbon as an efficient catalyst for direct CO_2 electroreduction to CO and hydrocarbons. *Angew. Chemie Int. Ed.* **2015**, *54*, 10758–10762. [CrossRef] [PubMed]
95. Su, P.; Iwase, K.; Nakanishi, S.; Hashimoto, K.; Kamiya, K. Nickel-Nitrogen-Modified Graphene: An Efficient Electrocatalyst for the Reduction of Carbon Dioxide to Carbon Monoxide. *Small* **2016**, *12*, 6083–6089. [CrossRef] [PubMed]
96. Jeong, H.; Balamurugan, M.; Choutipalli, V.S.K.; Jo, J.; Baik, H.; Subramanian, V.; Kim, M.; Sim, U.; Nam, K.T. Tris (2-benzimidazolylmethyl) amine-Directed Synthesis of Single-Atom Nickel Catalysts for Electrochemical CO Production from CO_2. *Chem. Eur. J.* **2018**, *24*, 18444–18454. [CrossRef]
97. Jiang, K.; Siahrostami, S.; Akey, A.J.; Li, Y.; Lu, Z.; Lattimer, J.; Hu, Y.; Stokes, C.; Gangishetty, M.; Chen, G. Transition-metal single atoms in a graphene shell as active centers for highly efficient artificial photosynthesis. *Chem* **2017**, *3*, 950–960. [CrossRef]
98. Jiang, K.; Siahrostami, S.; Zheng, T.; Hu, Y.; Hwang, S.; Stavitski, E.; Peng, Y.; Dynes, J.; Gangisetty, M.; Su, D. Isolated Ni single atoms in graphene nanosheets for high-performance CO_2 reduction. *Energy Environ. Sci.* **2018**, *11*, 893–903. [CrossRef]
99. Karapinar, D.; Huan, N.T.; Ranjbar, N.S.; Li, J.; Wakerley, D.; Touati, N.; Zanna, S.; Taverna, D.; Galvão, L.H.T.; Zitolo, A. Electroreduction of CO_2 on Single-Site Copper-Nitrogen-Doped Carbon Material: Selective Formation of Ethanol and Reversible Restructuration of the Metal Sites. *Angew. Chem. Int. Ed. Engl.* **2019**, *58*, 15098–15103. [CrossRef]
100. Gu, J.; Hsu, C.-S.; Bai, L.; Chen, H.M.; Hu, X. Atomically dispersed Fe^{3+} sites catalyze efficient CO_2 electroreduction to CO. *Science* **2019**, *364*, 1091–1094. [CrossRef]
101. Zhang, C.; Yang, S.; Wu, J.; Liu, M.; Yazdi, S.; Ren, M.; Sha, J.; Zhong, J.; Nie, K.; Jalilov, A.S. Electrochemical CO_2 Reduction with Atomic Iron-Dispersed on Nitrogen-Doped Graphene. *Adv. Energy Mater.* **2018**, *8*, 1703487. [CrossRef]
102. Zhu, Y.; Lv, K.; Wang, X.; Yang, H.; Zheng Xiao, G. 1D/2D nitrogen-doped carbon nanorod arrays/ultrathin carbon nanosheets: Outstanding catalysts for highly efficient electroreduction CO_2 to CO. *J. Mater. Chem. A* **2019**, *7*, 14895–14903. [CrossRef]
103. Zeng, L.; Shi, J.; Luo, J.; Chen, H. Silver sulfide anchored on reduced graphene oxide as a high-performance catalyst for CO_2 electroreduction. *J. Power Sources* **2018**, *398*, 83–90. [CrossRef]
104. Liu, S.; Tao, H.; Liu, Q.; Xu, Z.; Liu, Q.; Luo, J.-L. Rational design of silver sulfide nanowires for efficient CO_2 electroreduction in ionic liquid. *ACS Catal.* **2018**, *8*, 1469–1475. [CrossRef]
105. Li, H.; Xiao, N.; Hao, M.; Song, X.; Wang, Y.; Ji, Y.; Liu, C.; Li, C.; Guo, Z.; Zhang, F. Efficient CO_2 electroreduction over pyridinic-N active sites highly exposed on wrinkled porous carbon nanosheets. *Chem. Eng. J.* **2018**, *351*, 613–621. [CrossRef]
106. Share, K.; Lewis, J.; Oakes, L.; Carter, R.E.; Cohn, A.P.; Pint, C.L. Tungsten diselenide ($WSe_{2)}$ as a high capacity, low overpotential conversion electrode for sodium ion batteries. *RSC Adv.* **2015**, *5*, 101262–101267. [CrossRef]
107. Bissett, M.A.; Worrall, S.D.; Kinloch, I.A.; Dryfe, R.A.W. Comparison of two-dimensional transition metal dichalcogenides for electrochemical supercapacitors. *Electrochim. Acta* **2016**, *201*, 30–37. [CrossRef]
108. Wang, Q.H.; Kalantar-Zadeh, K.; Kis, A.; Coleman, J.N.; Strano, M.S. Electronics and optoelectronics of two-dimensional transition metal dichalcogenides. *Nat. Nanotechnol.* **2012**, *7*, 699. [CrossRef]
109. Eftekhari, A. Tungsten dichalcogenides (WS_2, WSe_2, and WTe_2): Materials chemistry and applications. *J. Mater. Chem. A* **2017**, *5*, 18299–18325. [CrossRef]
110. Zheng, Z.; Zhang, T.; Yao, J.; Zhang, Y.; Xu, J.; Yang, G. Flexible, transparent and ultra-broadband photodetector based on large-area WSe_2 film for wearable devices. *Nanotechnology* **2016**, *27*, 225501. [CrossRef]
111. Pumera, M.; Loo, A.H. Layered transition-metal dichalcogenides (MoS_2 and WS_2) for sensing and biosensing. *TrAC Trends Anal. Chem.* **2014**, *61*, 49–53. [CrossRef]
112. Chia, X.; Pumera, M. Layered transition metal dichalcogenide electrochemistry: Journey across the periodic table. *Chem. Soc. Rev.* **2018**, *47*, 5602–5613. [CrossRef] [PubMed]
113. Tedstone, A.A.; Lewis, D.J.; O'Brien, P. Synthesis, properties, and applications of transition metal-doped layered transition metal dichalcogenides. *Chem. Mater.* **2016**, *28*, 1965–1974. [CrossRef]

114. Asadi, M.; Kim, K.; Liu, C.; Addepalli, A.V.; Abbasi, P.; Yasaei, P.; Phillips, P.; Behranginia, A.; Cerrato, J.M.; Haasch, R. Nanostructured transition metal dichalcogenide electrocatalysts for CO_2 reduction in ionic liquid. *Science* **2016**, *353*, 467–470. [CrossRef] [PubMed]
115. Zhao, C.-X.; Zhang, G.-X.; Gao, W.; Jiang, Q. Single metal atoms regulated flexibly by a 2D InSe substrate for CO_2 reduction electrocatalysts. *J. Mater. Chem. A* **2019**, *7*, 8210–8217. [CrossRef]